MATERIALS CHEMISTRY
FRONTIERS

CHINESE CHEMICAL SOCIETY

ROYAL SOCIETY OF CHEMISTRY

RESEARCH ARTICLE

View Article Online
View Journal | View Issue

Cite this: *Mater. Chem. Front.*, 2021, **5**, 6530

Porous SiOC/SiC ceramics *via* an active-filler-catalyzed polymer-derived method†

Advaith V. Rau,[a] Ken Knott[b] and Kathy Lu *[a]

Received 11th May 2021,
Accepted 20th July 2021

DOI: 10.1039/d1qm00705j

rsc.li/frontiers-materials

In this study, bulk and porous SiOC materials were synthesized *via* a polymer-derived ceramic (PDC) method from a base polysiloxane (PSO) precursor and an iron (Fe) catalyst under an inert pyrolytic atmosphere. Fe catalyzes not only the formation and nucleation of β-SiC at lower temperatures but also promotes phase separation of the amorphous SiO_xC_y phase, compared to PDCs without the Fe catalyst. Samples with Fe pyrolyzed at 1100 °C have an appreciable β-SiC content compared to a negligible/unobservable β-SiC content in the corresponding Fe-less samples. Selective etching of the SiO_2 phase shows that Fe also induces segregation of the amorphous SiO_xC_y phase, yielding larger specific surface areas and gas sorption capability below 1300 °C. At 1500 °C, the pore structure changes to form interconnected networks due to the highly phase separated SiO_2 and β-SiC microstructure. A Gibbs free energy minimization method was used to determine the relative phase content of the pyrolyzed samples, with the effect of Fe quantified with simplified vapor–liquid–solid (VLS), solid–liquid–solid (SLS), and classical nucleation theories.

1. Introduction

Polymer-derived ceramics (PDCs) are a class of ceramics that offer a high degree of synthetic control over imbued microstructures and properties by tailoring the polymer precursor chemistry and composition.[1–4] PDCs are emerging as a popular system for porous ceramic fabrication as pore structure, size, and distribution can be modified by methods such as use of sacrificial fillers,[5,6] phase separation from polymer precursors,[7–9] replica templates,[10,11] incorporation of polymeric additives,[12,13] and selective etching of as-formed ceramic phases by controlling pyrolytic atmospheres and temperatures.[13–16] Porous ceramics have applications including catalyst supports, electrodes, gas separation membranes, thermal insulation, and lightweight materials,[17,18] among others. In particular, porous silicon oxycarbide (SiOC) ceramics have garnered interest for their excellent thermal stability,[19–21] corrosion resistance,[22] and thermomechanical properties[3,23,24] in potential high-temperature, aerospace, and abrasive applications.[2,3,25] Through pyrolytic conversion of silicon-rich polymer precursor(s), a wide range of SiO_xC_y ceramics can be produced with varying Si/O/C contents through rational control of precursor composition, precursor architecture, and pyrolysis temperature, ultimately tailoring the phase and microstructure evolution.

In a typical PDC-SiOC synthesis method, the polymer-to-ceramic phase transformation initiates at 600 °C with SiOC phases predominantly existing up to around 1000 °C, which then gradually segregate to SiO_2, β-SiC, and free carbon phases around 1300 °C.[26] SiC prominently crystallizes at ~1500 °C from the carbothermal reduction of SiO_2 and free carbon phases present in the SiOC matrix[26,27] – these processing temperatures are generally needed to significantly realize a prominent SiC phase. Achieving bulk or porous SiC ceramics *via* PDCs thus remains an issue due to the high temperatures needed, low ceramic yield, and defect formation due to gas evolution and shrinkage during pyrolysis. The viability of bulk/porous SiC ceramics from polysiloxane precursors depends on the ability to lower the critical nucleation temperature for SiC.

Transition metal fillers have been shown to reduce the formation temperature of SiC through generation of transition metal carbides, silicides, and oxides. In addition to imparting ancillary properties for applications in catalysis[28,29] and magnetics,[30–32] transition metal active fillers such as Al,[33–37] Ce,[29] Fe,[30–32,38,39] Hf,[40–44] Ni,[45] Ti,[46–50] V,[38,46] and Zr[20,51–53] have been incorporated into silicon-rich polymer precursors to improve or alter phase development. Based on some initial predictions by Ionescu *et al.*,[38] these transition metal fillers can be further classified based on the metallic byproducts after pyrolytic conversion: metals that are reduced back to the elemental state, such as Au,[38] Pd,[54] Pt,[28] and metals that form oxides, silicides, or carbides such as Fe,[30–32,38] Mg,[55] Ni,[45,56]

---

[a] *Department of Materials Science and Engineering, Virginia Polytechnic Institute and State University, Blacksburg, Virginia, 24061, USA. E-mail: klu@vt.edu*
[b] *Department of Chemistry, Virginia Polytechnic Institute and State University, Blacksburg, Virginia, 24061, USA*

† Electronic supplementary information (ESI) available. See DOI: 10.1039/d1qm00705j

Ti,[47–49] Hf,[43] and Zr.[52] The relative stability of a metal oxide/silicide/carbide is dependent on the pyrolytic temperature and atmosphere as well as the precursor chemistry. In most of the mentioned systems, SiC nucleation was observed at lower temperatures than from an unmodified polymer system. Elucidation of the reaction pathways in which the nucleation temperature of SiC is reduced is critical. As of yet, a rigorous understanding of the reaction steps and thermodynamic modelling has not yet been performed.

Fe is of interest for its ability to generate β-SiC at low temperatures, but previous studies used a relatively high weight content of Fe that led to higher iron silicide formation.[30] At high weight ratios of Fe to the base polymer, the catalytic effects of Fe were masked or overshadowed by secondary phase formation. By increasing the iron acetylacetonate (Fe(acac)$_3$) concentration, SiC was shown to form at 1300 °C with the simultaneous formation of iron silicides (Fe_xSi_y); Fe_xSi_y formation also induced magnetic functionality to the SiOC nanocomposite.[30,31] The presence of Fe in the polymer precursor fostered the carbothermal reduction reaction by formation of Fe_xSi_y, Fe_xO_y, and Fe_xC_y crystallites in the SiOC matrix.[57,58] It has also been reported that β-SiC is unstable in the presence of high concentrations of transition metals,[56] which could be mitigated at a lower Fe content and has yet to be fully studied.

In addition to metallic fillers, organic fillers have been considered to mitigate processing issues common to PDCs including porosity, ceramic yield, and volume shrinkage. In general, the ceramic yield is on the order of 70%, which can hamper the viability of PDCs in large-scale applications. In a previous study, siloxane-based fillers were incorporated into a polysiloxane matrix to improve the ceramic yield.[12] Notably, octavinyl-polyhedral oligomeric silsesquioxane (POSS) – a caged siloxane additive – was shown to significantly improve the ceramic yield due to enhanced SiO_2 nucleation and formation.[12] This SiO_2-rich precursor can be utilized in Fe-catalyzed systems to improve ceramic yield and drive β-SiC phase formation through carbothermal reduction of POSS-derived SiO_2 domains.

In this study, a low weight percent of Fe(acac)$_3$ was incorporated into a polysiloxane matrix along with a SiO_2-rich additive to investigate low temperature formation of SiC. Varying ratios of PSO to POSS were used to investigate and understand the catalytic effect of Fe in regard to β-SiC crystallization. The effects of composition and pyrolysis temperature were investigated using X-ray diffraction (XRD) and nuclear magnetic resonance (NMR) spectroscopy. The underlying thermodynamic and reaction pathways were modeled in order to predict the phase fractions in Fe-catalyzed SiOC systems and understand the mechanism of Fe-catalyzed β-SiC evolution.

2. Experimental

2.1 Materials

A commercially available polysiloxane Polyramic SPR-684 (PSO, $[-Si(C_5H_6)_2O-]_3[-Si(CH_3)(H)O-]_2[-Si(CH_3)(CH{=}CH_2)O-]_2$, Starfire Systems, Inc., Glenville, NY) was used as the base polymer precursor. Octavinyl-polyhedral oligomeric silsequioxane (POSS, OL1170, Hybrid Plastics, Hattiesburg, MS) was used as the additive in the base polymer, and iron(III) acetylacetonate (Fe(acac)$_3$, 97%, Sigma-Aldrich, St. Louis, MO) was chosen as the active filler. A 2.1% platinum–divinyltetramethyldisiloxane complex in xylene (Pt catalyst, Gelest, Inc.) was used to crosslink the polymer precursor samples. Acetone (Fisher Scientific, technical grade, Waltham, MA) was used as a solvent to facilitate mixing and dispersion. Argon (Ar, Industrial Grade, AirGas, Radford, VA) was used as the pyrolysis atmosphere. Hydrofluoric acid (HF, 49% (aq), Avantor Specialty Materials Inc., Radnor, PA) was used as an etchant. Nanopure water (18.2 MΩ cm) was used throughout the study. All chemicals were used as received without further purification.

2.2 Sample preparation

Polymer precursor solutions were prepared by mechanically stirring PSO with 0, 5, 10, or 15 wt% POSS (POSS content relative to total mass of PSO and POSS), 1 wt% Fe^{3+} (weight percent of Fe – roughly 6.41 wt% Fe(acac)$_3$ – relative to base PSO), and 1 wt% Pt catalyst (relative to PSO) until completely homogenous. For solutions containing POSS or Fe(acac)$_3$, 5–10 mL of acetone was added to fully dissolve POSS and Fe(acac)$_3$ and to promote thorough mixing with the polymer precursor. A blank group without any Fe(acac)$_3$ or POSS was prepared similarly but without the addition of acetone. The solutions were thoroughly degassed under vacuum to remove air bubbles and the solvent, cast to cylindrical molds, degassed again, and cured at 60 °C for 12 h and then 120 °C for 12 h. The green bodies were sectioned into approximately Φ 12 mm × 5 mm specimens, polished and edges slightly beveled up to 1200 grit, and placed in a tube furnace (1730-12 Horizontal Tube Furnace, CM Furnaces, Inc., Bloomfield, NJ). Under an Ar atmosphere with a flow rate of $\sim$500 cm^3 min^{-1}, the green bodies were pyrolyzed at either 1100 °C, 1300 °C, or 1500 °C by heating to the peak temperature at 2 °C min^{-1}, holding for 2 h, and cooling to ambient temperature at 2 °C min^{-1}. The pyrolyzed samples were denoted as xPOSS–1Fe or xPOSS–0Fe (x = 0, 5, 10, or 15) for the samples with and without the Fe catalyst, respectively. The pyrolyzed samples were broken into $\sim$5 mm pieces and etched in a stirring 20% HF (aq) solution at less than 10 wt% for at least 96 h until no mass loss was observed. Etched samples were thoroughly cleaned in nanopure water and dried for 12 h at 120 °C.

2.3 Characterization

The ceramic yield and volume shrinkage were calculated from changes in mass and volume, respectively, between the green bodies and pyrolyzed samples. Phase compositions were analyzed with an X'Pert PRO diffractometer (PANalytical B.V., EA Almelo, The Netherlands) with Cu Kα radiation between 2θ = 10–100 °C with a scanning rate of 0.05° s^{-1}. Sample compositions were determined *via* combustion for C and optical emission spectroscopy (ICP-OES, Agilent 5110 ICP-OES, Agilent Technologies, Inc., Santa Clara, CA) for Si and Fe. Carbon combustion analysis was performed by Galbraith Laboratories, Inc. (Knoxville, TN). ICP-OES samples were prepared by borate fusion followed by acid digestion and dilution (see S1, ESI†). The oxygen content was taken as the difference between the calculated masses for C, Si, and Fe and the total sample mass. The specific surface area, pore volume, and pore size distribution of the etched samples were evaluated by nitrogen adsorption at 77 K (Quantachrome Autosorb-1, Quantachrome Instruments, Boynton Beach, FL). Samples were degassed under vacuum at 300 °C for 12 h prior to analysis. Non-Local Density Functional Theory (NLDFT) was applied to the adsorption branch with a cylindrical pore structure based on a silica adsorbate model. Single pulse MAS NMR spectra were measured using a Bruker Avance III NMR spectrometer at a frequency of 59.627 MHz for ^{29}Si and a 4 mm rotor at a MAS frequency of 10 kHz. The number of scans was 2500 or 5000. Single-pulse experiments used a 2.5 μs pulse width and 60 s recycle delay. ^{29}Si was calibrated by an external standard TMS (0 ppm).

3. Results and discussion

3.1 Phase evolution

In pure SiOC systems, β-SiC formation has been postulated to occur through two processes: phase separation of amorphous SiOC or carbothermal reduction of phase separated SiO_2 and C.[59] In the former, phase separation of amorphous SiOC occurs from 1100 °C to 1500 °C to yield SiO_2, β-SiC, and graphitic/turbostratic C.[30,59,60]

$$2SiOC \rightarrow SiO_2(am) + SiC(\beta) + C_{graphite} \tag{1}$$

At higher pyrolytic temperatures than 1500 °C, β-SiC is formed through carbothermal reduction of SiO_2 with evolution of CO:[26,27,30,59]

$$SiO_2 + 3C_{graphite} \rightarrow SiC(\beta) + 2CO(g) \tag{2}$$

The carbothermal reduction reaction proceeds through two steps, in which the second reaction is the rate-limiting step,

$$SiO_2 + C_{graphite} \rightarrow SiO + CO(g) \tag{3}$$

$$SiO + 2C_{graphite} \rightarrow SiC(\beta) + CO(g) \tag{4}$$

However, the presence of Fe lowers the critical temperature for β-SiC formation and has been postulated to occur through the formation of iron silicides (Fe_xSi_y). The pathway for Fe_xSi_y evolution – most prevalently Fe_3Si between 1000 °C and 1300 °C and Fe_5Si_3 above 1300 °C – has been proposed to proceed through the phase separation and formation of FeO_x and Fe_3C intermediates.[30,38] Upon pyrolytic conversion of the polymeric green bodies beginning at 600 °C, a nominally single-phase SiFeOC undergoes phase separation into SiOC and FeO_x. In another study, Fe_3O_4 phases have been observed up to 600 °C in an Fe-modified polycarbosilane system.[32] However, FeO_x is unstable in carbon-rich environments at this temperature and forms Fe_3C *via* carbothermal reduction. The conversion of Fe_3C to Fe_3Si occurs above ~770 °C as Fe_3C is unstable in carburizing atmospheres,[38,61] and evolves into Fe_3Si upon reaction with SiO_2 and C:

$$Fe_3C + SiO_2 + C_{graphite} \rightarrow Fe_3Si + 2CO(g) \tag{5}$$

Alternatively, it has been proposed that Fe_3C decomposes to elemental iron and graphite prior to formation of Fe_3Si.[38] As the Gibbs free energy change for the carbothermal reduction of FeO_x to Fe_3C is slightly lower than that of FeO_x to Fe,[30,38] it may be reasonably assumed that Fe_3C rather than elemental Fe is the ferrous intermediate generated prior to iron silicide formation. The intrinsic decomposition of SiOC in eqn (1), removal of SiO_2 and C by-products in eqn (5), and added decomposition of the SiOC phase by Fe_3C can promote the growth of β-SiC. In the last scenario, such phase separation would also yield gaseous CO and SiO byproducts.[31] Above 1300 °C, Fe_3Si can further induce crystallization of β-SiC through the following reaction:[30]

$$Fe_3Si + C_{graphite} \rightarrow Fe_5Si_3 + SiC(\beta) \tag{6}$$

The effect of Fe and pyrolysis temperature are readily apparent in the XRD spectra (Fig. 1). The spectra were normalized with respect to the ~35.5° peak, which was indexed as the (111) plane of β-SiC in order to qualitatively assess the effects of Fe and POSS contents and pyrolysis temperature. The peaks at 41°, 60°, and 72° were indexed as the (200), (220), and (311) planes of β-SiC, respectively. Broad graphite peaks were observed between 25° and 28° and at 44°. Minor reflections corresponding to iron silicides (Fe_3Si at 1100 °C, Fe_5Si_3 at 1300 °C and 1500 °C) were observed in the Fe-containing samples between 45° and 47°. At 1100 °C (Fig. 1(a)), the catalyzing effect of Fe is immediately notable – the *x*POSS–0Fe samples remain largely amorphous with little-to-no evidence of crystallized β-SiC, which agrees with prior studies.[12,45,62] The addition of Fe yields prominent crystallization of both graphite and β-SiC in all samples. At 1300 °C (Fig. 1(b)), β-SiC crystallization has initiated in the *x*POSS–0Fe samples, as evidenced by broader peaks (~32°–38°) that are indicative of smaller crystallites. With the addition of Fe, the β-SiC phase is more prominent and the relative amorphous content decreases compared to the Fe-less samples. At 1500 °C (Fig. 1(c)), the sharpness and strength of the β-SiC peaks in the *x*POSS–1Fe samples demonstrate substantial β-SiC crystallization as compared to unmodified samples. An amorphous $SiO_2/SiO_xC_y/C$ halo in the 20°–30° region is evident in the Fe-less samples at all temperatures and in the Fe-containing samples at 1100 °C and 1300 °C.

At both 1100 °C and 1300 °C, POSS does not influence β-SiC formation and predominantly contributes to more amorphous SiO_2 content. At 1500 °C, POSS still remains a small contributor to amorphous SiO_2 formation in 0POSS–1Fe, 5POSS–1Fe, and all *x*POSS–0Fe samples; however, in 10POSS–1Fe and 15POSS–1Fe samples, the β-SiC peak at ~35.5° is much sharper and stronger with a smaller graphitic carbon peak at ~26°. At these POSS concentrations, the carbothermal reduction reaction of SiO_2 and C to β-SiC proceeds to a greater extent, potentially due to a higher probability of contact between SiO_2 and free C domains in the SiOC microstructure and the presence of better refined Fe-catalyzed β-SiC seeds/nucleation sites. Further β-SiC

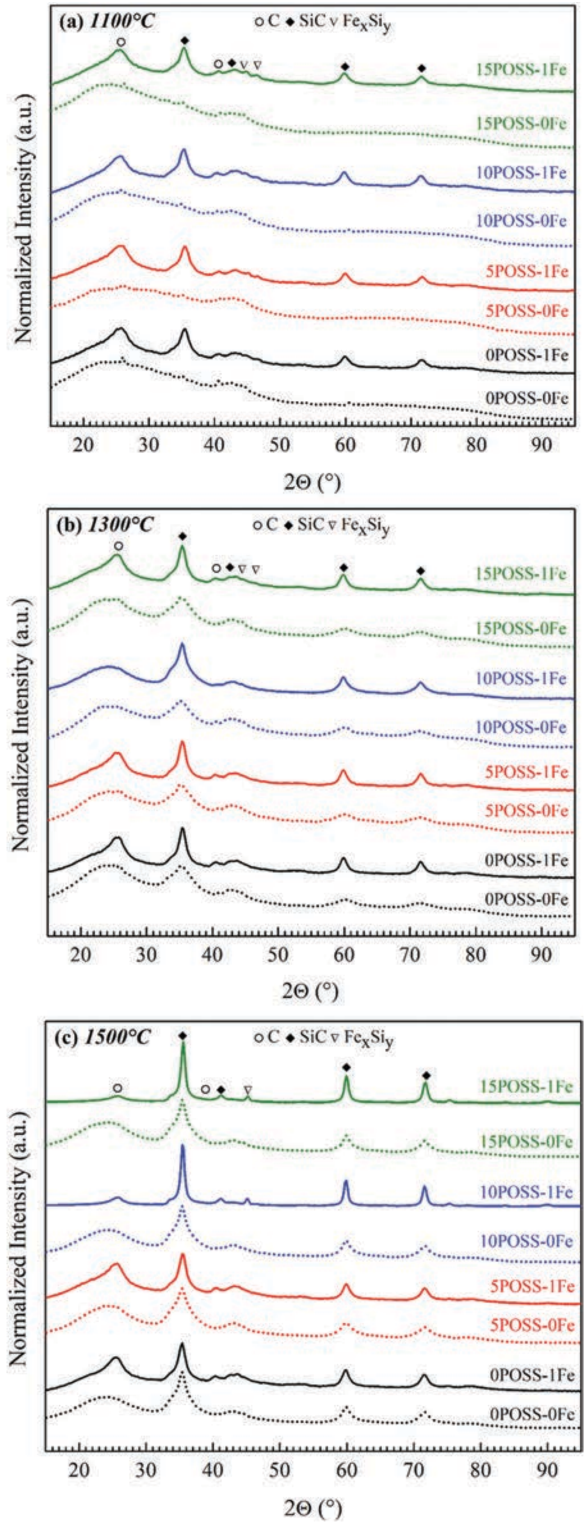

Fig. 1 Normalized XRD spectra of pyrolyzed POSS–Fe samples in Ar at (a) 1100 °C, (b) 1300 °C, and (c) 1500 °C of 0% (black), 5% (red), 10% (blue), and 15% (green) POSS–Fe samples. Solid lines refer to *x*POSS–1Fe samples, dotted lines refer to *x*POSS–0Fe samples. Spectra were normalized with respect to the intensity of the (111) β-SiC peak at ~35.5°.

catalyzation from the conversion of Fe_3Si to Fe_5Si_3 also contributes to the enhanced phase refinement.

Compared to the spectra for the Fe-free samples, the graphite and β-SiC peaks are much sharper in the Fe-containing samples at each temperature, indicating a larger and more refined crystallite size. The sharpening of the graphitic peak at ~26° further indicates enhanced graphitization compared to the relatively disordered carbon in the Fe-less samples. The Scherrer equation can be used to estimate crystallite size (D) based on peak broadening (β):

$$D = \frac{0.9\lambda}{\beta \cos\theta_B} \quad (7)$$

in which λ is the wavelength of the incident Cu Kα X-rays and θ_B is the diffraction Bragg angle. Table 1 provides the mean crystallite size for β-SiC at 1100 °C, 1300 °C, and 1500 °C for the different POSS concentrations. Little-to-no β-SiC could be detected at 1100 °C in the *x*POSS–0Fe samples, so the crystallite size is not calculated.

The β-SiC mean crystallite size increases with the pyrolytic temperature in both Fe-containing and Fe-free samples as expected, due to the β-SiC formation from both SiO_xC_y phase separation and carbothermal reduction of SiO_2. At all temperatures and POSS contents, the β-SiC crystallite size is larger in the Fe-containing samples. This further elucidates that Fe is responsible for β-SiC nucleation below 1100 °C. These small nuclei in the Si–O–C microstructure provide energetically favorable sites for further nucleation/crystal growth and reduce the energetic barrier for β-SiC crystallization. At 1100 °C and 1300 °C, POSS does not appear to contribute to β-SiC crystallite growth. For the *x*POSS–0Fe samples, the increase in the β-SiC crystallite size is mainly attributed to the SiOC phase separation and limited carbothermal reduction between 1100 °C and 1500 °C. For the *x*POSS–1Fe samples, a relatively small change in the crystallite size between 1100 °C and 1300 °C indicates that the majority of the SiO_xC_y phase separation has occurred by 1100 °C, with the process being nearly complete by 1300 °C. Between 1300 °C and 1500 °C, the mean crystallite size for 0POSS–1Fe and 5POSS–1Fe is relatively constant; however, the crystallite size nearly doubles in the 10POSS–1Fe and 15POSS–1Fe samples. It is possible that the SiO_2 aggregation occurs due to a higher degree of proximity among SiO_2 domains evolved from either POSS degradation or SiO_xC_y phase separation. These larger domains could yield larger β-SiC crystallites upon carbothermal reduction. In a similar vein, the increased crystallite size could also occur from coarsening of β-SiC nanodomains formed after carbothermal reduction of SiO_2 nanodomains. As a higher POSS content increases the contact probability between SiO_2 and free C and intrinsic proximity of SiO_2 nanodomains, the evolved β-SiC crystallites have a higher propensity to coalesce.

^{29}Si NMR was performed to quantitatively determine the relative amounts of SiO_2, β-SiC, and amorphous SiO_xC_y (SiO_2, $SiO_{3/2}C_{1/4}$, $SiOC_{1/2}$, and $SiO_{1/2}C_{3/4}$) present in the pyrolyzed 0POSS–0Fe and 0POSS–1Fe samples. Due to the unique chemical environment around each Si nucleus, the amorphous SiO_xC_y phases can be differentiated. Fig. 2 depicts the ^{29}Si NMR spectra of the 0POSS–0Fe (dotted line) and 0POSS–1Fe (solid lines) samples pyrolyzed at 1100 °C (black), 1300 °C (red), and 1500 °C (blue). The chemical shifts for SiO_2, $SiO_{3/2}C_{1/4}$, $SiOC_{1/2}$,

Table 1 Mean crystallite size of β-SiC after pyrolysis at 1100 °C, 1300 °C, and 1500 °C. Average and standard deviation values were calculated from crystallite sizes determined from β-SiC peaks at 35.5°, 60°, and 72°

	Mean β-SiC crystallite Size (nm)							
	0POSS		5POSS		10POSS		15POSS	
Temp. (°C)	0Fe	1Fe	0Fe	1Fe	0Fe	1Fe	0Fe	1Fe
1100	—	5.2 ± 0.5	—	6.1 ± 0.6	—	6.0 ± 0.4	—	5.9 ± 0.3
1300	2.8 ± 0.3	7.2 ± 0.6	2.9 ± 0.2	6.9 ± 0.5	3.2 ± 0.5	7.2 ± 0.6	2.9 ± 0.3	6.6 ± 0.4
1500	5.4 ± 0.6	7.0 ± 0.4	4.3 ± 0.5	6.9 ± 0.5	5.6 ± 0.7	12.8 ± 0.6	5.8 ± 0.8	11.8 ± 0.6

$SiO_{1/2}C_{3/4}$, and β-SiC of ∼−107, −70, −34, 7, and −11 ppm, respectively, were referenced from previous literature and studies.[63–65] At 1100 °C, the 0POSS–0Fe sample has prominent amorphous SiO_2 and SiO_xC_y contents; however, upon addition of Fe there is notable phase separation to SiO_2 and β-SiC. At 1300 °C, the Fe-less system has undergone phase separation as well, but there is a higher proportion of β-SiC in the 0POSS–1Fe sample from growth of previously nucleated β-SiC seeds. At 1500 °C, both samples are predominantly β-SiC but the 0POSS–0Fe sample still has some residual SiO_2.

The relative phase fractions were obtained by fitting five Gaussian peaks to aforementioned chemical shifts to the experimental spectra (see S2, ESI†) and are presented in Table 2. From the calculated phase fractions and qualitatively from the NMR spectra, Fe not only catalyzes β-SiC formation but also induces phase separation of the amorphous SiOC matrix, which has not been previously reported. In the unmodified SiOC systems, phase separation and carbothermal reduction are competing processes around 1300 °C. With the addition of Fe, the decomposition of the amorphous SiOC matrix has nearly completed by 1300 °C so there is more amorphous SiO_2 available to reduce to β-SiC. SiO_2 separation from the SiO_xC_y phase can also attribute to nanodomain aggregation to explain the larger β-SiC crystallite sizes in the 10POSS–1Fe and 15POSS–1Fe samples pyrolyzed at 1500 °C. Therefore, Fe has been observed to not only lower the critical nucleation temperature of β-SiC and induce graphitization of free C, but also have an unexplored role in phase separation of amorphous SiO_xC_y. Because the concentration of Fe_3Si is very low, it could not be reasonably discerned in the ^{29}Si NMR spectra – this is corroborated by the low Fe content observed from elemental analysis. In the 0POSS–1Fe_1500 sample, the spectrum had high background noise that prevented more accurate peak-fitting. While some of the SiO_xC_y intermediates are not expected to be appreciably present in this condition, fitting peaks were forced through these peak centers as it was not readily apparent that these intermediates are present or absent.

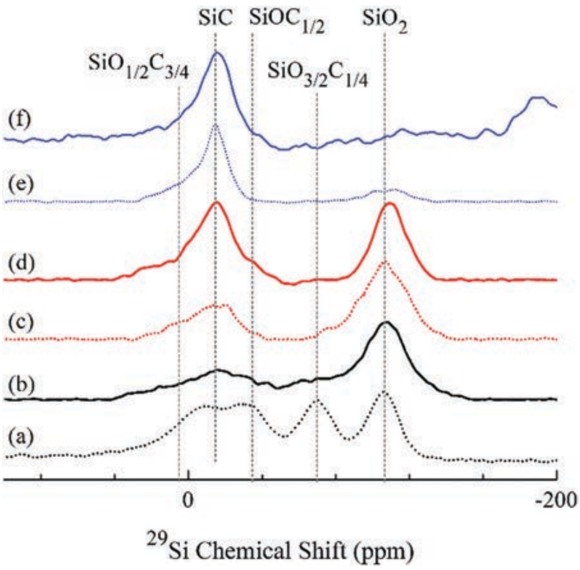

Fig. 2 Normalized ^{29}Si NMR spectra of (a) 0POSS–0Fe (1100 °C), (b) 0POSS–1Fe (1100 °C), (c) 0POSS–0Fe (1300 °C), (d) 0POSS–1Fe (1300 °C), (e) 0POSS–0Fe (1500 °C), and (f) 0POSS–1Fe (1500 °C). Peaks I, II, III, IV, and V correspond to SiO_2 (∼−107 ppm), $SiO_{3/2}C_{1/4}$ (∼−70 ppm), $SiOC_{1/2}$ (∼−34 ppm), $SiO_{1/2}C_{3/4}$ (∼7 ppm), and SiC (∼−11 ppm) structural units, respectively. Spectra were normalized with respect to the most intense peak.

3.2 Physical properties

Fig. 3 depicts the ceramic yield (black) and volumetric shrinkage (blue) of the *x*POSS–0Fe (dotted) and *x*POSS–1Fe (solid) samples. The addition of POSS yields expected trends of increasing ceramic yield and decreasing volume shrinkage per an earlier study.[12] In general, the mass and volume losses of the Fe-containing samples are greater than those of the Fe-less samples. This may be attributed to CO evolution from the SiO_2 and C consumption in the Fe_3C to Fe_3Si conversion in eqn (5). Between 1100 °C and 1300 °C, the yield remains relatively constant, indicating that any phase evolution is predominantly due to the phase separation of the amorphous SiOC matrix and there is no appreciable contribution from β-SiC formation *via* carbothermal reduction of SiO_2 and free C. However, at 1500 °C, there is significant mass loss (yield decrease) in the presence of Fe while

Table 2 Calculated phase fractions of SiO_2, $SiO_{3/2}C_{1/4}$, $SiOC_{1/2}$, $SiO_{1/2}C_{3/4}$, and β-SiC from Gaussian peak fitting of ^{29}Si NMR spectra in Fig. 2 and the corresponding calculated (NMR) chemical compositions

	Phase content of SiO_xC_y species (%)					Composition
Sample	SiO_2	$SiO_{3/2}C_{1/4}$	$SiOC_{1/2}$	$SiO_{1/2}C_{3/4}$	SiC	(peak fitting)
0POSS–0Fe_1100	25.0	22.5	30.3	12.3	9.8	$SiO_{1.20}C_{0.40}$
0POSS–1Fe_1100	56.6	13.3	8.7	5.4	16.1	$SiO_{1.44}C_{0.28}$
0POSS-0Fe_1300	60	6.3	0.5	5.5	28.2	$SiO_{1.30}C_{0.33}$
0POSS–1Fe_1300	43.7	0.5	0.5	8.5	46.9	$SiO_{0.90}C_{0.52}$
0POSS–0Fe_1500	13.3	0.7	3.6	9.3	73.1	$SiO_{0.35}C_{0.79}$
0POSS–1Fe_1500	0.8	2.1	10.6	14.1	72.4	$SiO_{0.21}C_{0.85}$

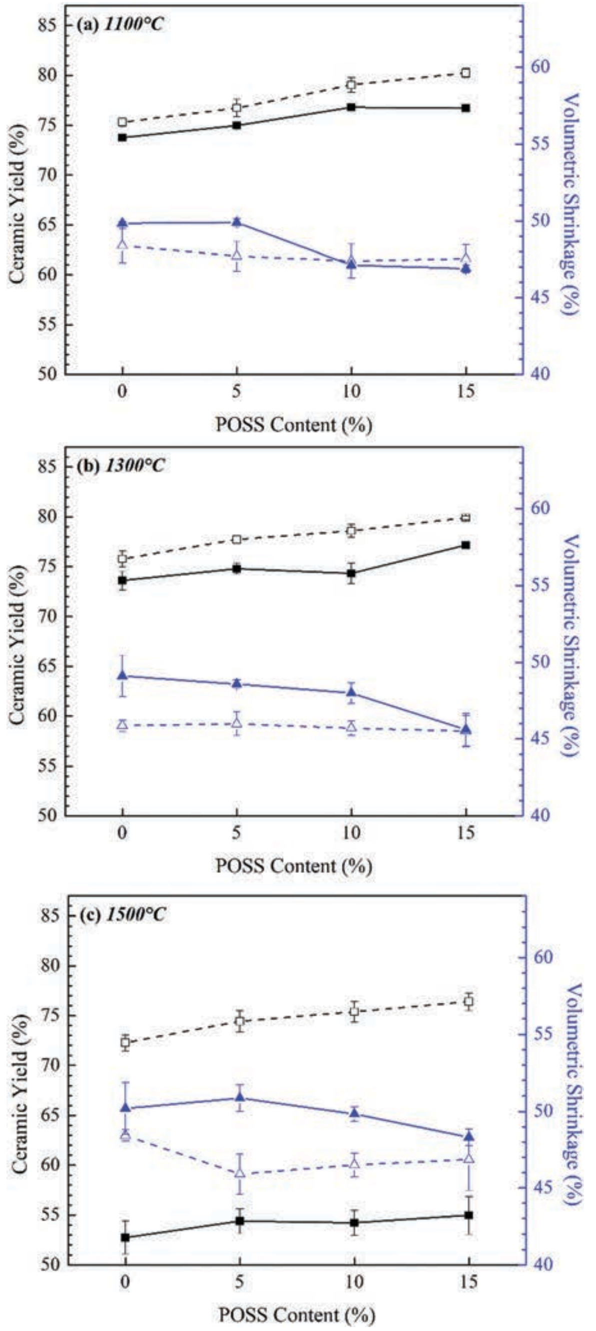

Fig. 3 Ceramic yield (black) and volume shrinkage (blue) of pyrolyzed samples at (a) 1100 °C, (b) 1300 °C, and (c) 1500 °C. Solid lines refer to *x*POSS–1Fe samples, dotted lines refer to *x*POSS–0Fe samples. Data points are averages of 4–6 samples and error bars indicate standard deviation.

only a slight decrease is observed in the absence of Fe. As shown in Fig. 1, the Fe-containing samples at 1500 °C have more β-SiC phase so the mass loss should correspond to the crystallization and growth of β-SiC. The majority of β-SiC formation and mass loss is due to increased carbothermal reduction rate spurred by Fe-induced SiO_2 segregation. In addition to CO evolved per eqn (2), additional mass loss above 1400 °C may be attributed to the volatilization of SiO_2 and β-SiC phases:[26]

$$2SiO_2(am) + SiC(\beta) \rightarrow 3SiO(g) + CO(g) \qquad (8)$$

Saha *et al.* reported that crystallization kinetics and mass loss in SiOC systems are codependent and a function of the vapor pressure of CO in the system.[26] The higher β-SiC concentration at lower temperatures in the Fe-catalyzed samples can provide additional forward driving force for eqn (8) and cause additional mass loss. Notably, the volumetric shrinkage of the Fe-containing sample does not significantly increase at 1500 °C in a similar manner to the mass loss. These samples must then have pore formation as SiO and CO are evolved through eqn (3) and (8) but the rigidity of the β-SiC network inhibits spontaneous sample shrinkage. Overall, the volumetric shrinkage for the Fe-containing samples is generally constant across the temperatures studied, indicating that any prominent mass loss events could yield some intrinsic porosity.

3.3 Pore size and specific surface area of porous SiOC/SiC

Porous SiOC/SiC structures are formed by selective etching of SiO_2 domains with HF. As SiO_xC_y and SiC (more specifically the Si–C bonds) are resistant to HF, mass loss and pore formation can be attributed to the size, concentration, and distribution of the SiO_2 domains, which are removed through the following reaction with a molar excess of HF:

$$SiO_2 + 6HF \rightarrow H_2SiF_6 + 2H_2O \qquad (9)$$

Fig. 4 shows the nitrogen sorption isotherms and pore size distributions for *x*POSS–0Fe and *x*POSS–1Fe pyrolyzed at 1100 °C, 1300 °C, and 1500 °C after HF etching. The largest disparity is visible at 1100 °C, with the HF-etched 0POSS–0Fe showing almost no adsorptive behavior (6.3 $cm^3\ g^{-1}$ at $P/P_0 \sim 1$) while the HF-etched 0POSS–1Fe has a gas adsorption volume of 206.7 $cm^3\ g^{-1}$ at $P/P_0 \sim 1$. Even though SiO_2 is present in the 0POSS–0Fe sample at 1100 °C per the XRD and NMR results in Fig. 1 and 2, the SiO_2 domains are most likely too small (less than 2–3 nm) to be accessed or etched by the HF solution. Due to the phase separation in the presence of Fe, the SiO_2 domains are more developed and thus can be successfully etched by HF. At 1300 °C, phase separation has proceeded in the 0POSS–0Fe samples so sufficiently sized SiO_2 nanodomains can be etched. The gas adsorption volumes for 0POSS–0Fe and 0POSS–1Fe at 1300 °C are 86.4 and 257.2 $cm^3\ g^{-1}$, respectively, at $P/P_0 \sim 1$. At 1500 °C, the gas adsorption volumes for 0POSS–0Fe and 0POSS–1Fe are 230.23 and 262.9 $cm^3\ g^{-1}$, respectively. As expected, the gas adsorption volume increases with temperature in parallel with the growth of the amorphous SiO_2 phase. The volume adsorption difference between *x*POSS–0Fe and *x*POSS–1Fe samples decreases with increasing temperature, with nearly identical adsorption volumes at 1500 °C although the pore structure is different. Up to 1300 °C, Fe-catalyzed SiOC phase separation is the predominant mechanism for SiO_2 formation. From 1300–1500 °C, intrinsic SiOC phase separation becomes more substantial and eventually the Fe catalyst effect becomes insignificant for SiO_2 formation. In addition, SiO_2 and C carbothermal reaction intensifies at high temperatures based on eqn (2), which can offset the Fe catalyst effect.

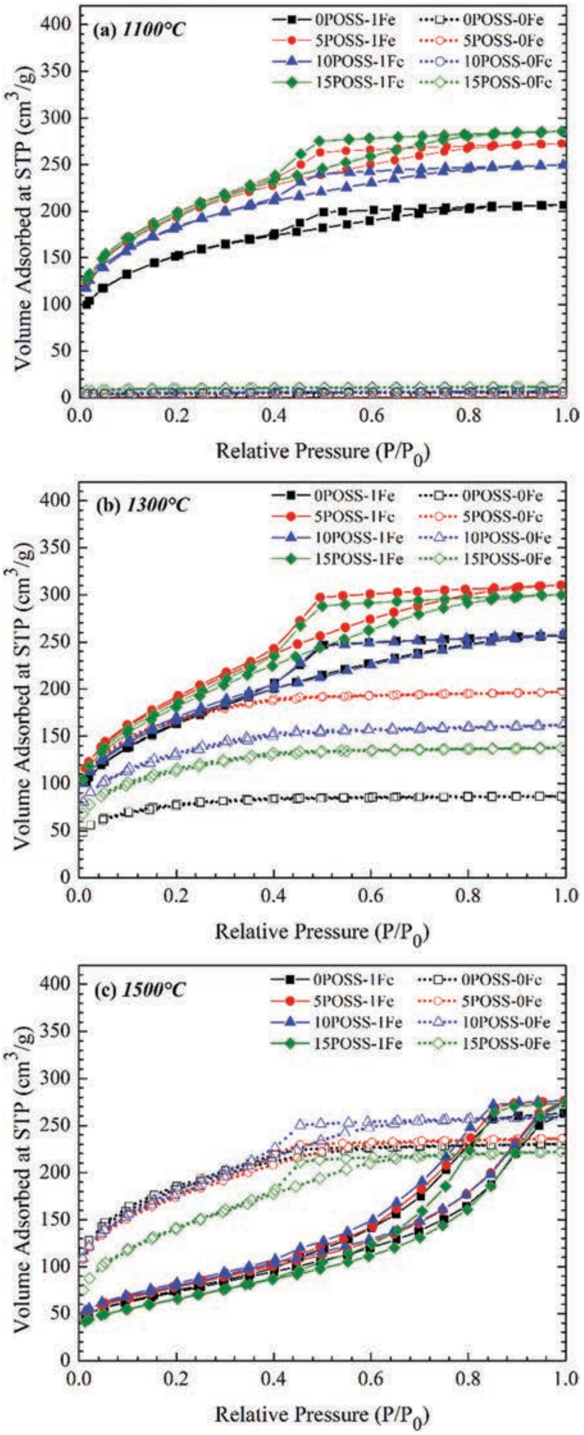

Fig. 4 Nitrogen sorption isotherms of HF-etched 0% (black), 5% (blue), 10% (red), and 15% (green) POSS samples with Fe (solid line/solid symbols) and without Fe (dotted line/hollow symbols) at (a) 1100 °C, (b) 1300 °C, and (c) 1500 °C.

In general, the addition of POSS increases the gas adsorption volume at 1100 °C and 1300 °C but with minimal difference at 1500 °C for the samples with Fe. At 1100 °C, the gas adsorption volumes of 0POSS–1Fe, 5POSS–1Fe, 10POSS–1Fe, and 15POSS–1Fe are 206.7, 272.6, 249.6, and 285.8 cm^3 g^{-1}, respectively. At 1300 °C, the gas adsorption volumes of 0POSS–1Fe, 5POSS–1Fe, 10POSS–1Fe, and 15POSS–1Fe are 257.2, 310.3, 258.0, and 299.9 cm^3 g^{-1}, respectively. The decrease between 5% and 10% POSS could be due to the aggregation of either SiO_2 nanodomains from POSS or intrinsically formed SiO_2 domains.[12] At 1500 °C, the gas adsorption volumes of 0POSS–1Fe, 5POSS–1Fe, 10POSS–1Fe, and 15POSS–1Fe are 262.9, 276.4, 276.2, and 274.1 cm^3 g^{-1}, respectively. Because the mesoporous structure observed at lower temperatures devolves into a wider pore distribution and forms interconnected channels due to SiO_2 domain aggregation, the overall gas sorption behavior becomes independent of the POSS content. Notably, the sorption curves for 0POSS–0Fe at all temperatures and 0POSS–1Fe at 1100 °C and 1300 °C show similar H4-type hysteresis behaviors, which is indicative of narrow slit-like pores. The sorption curve for 0POSS–1Fe at 1500 °C shows H2-type hysteresis behavior, indicating there are both wide and narrow pores with possible interconnecting channels.

Pore size distributions are calculated from the adsorption branch, assuming cylindrical pore structures based on the NLDFT theory (Fig. 5). While all samples except 0POSS–1Fe-1500 °C exhibit slit-like pores, the small library of NLDFT on SiO_2 adsorbate models precludes analysis with either slit or hybrid slit/cylindrical pore structures. The pore sizes for *x*POSS–0Fe at 1300 °C and 1500 °C and *x*POSS–1Fe at 1100 °C and 1300 °C are all generally under 10 nm with most pores between 3–6 nm. As the SiO_2 nanodomains in the *x*POSS–0Fe samples at 1100 °C are sufficiently small/negligible to resist HF etching, no pores are detected through the NLDFT analysis. The *x*POSS–1Fe samples at 1500 °C lose the mesoporous structure observed in the other samples and have a wide distribution from 4 nm to over 20 nm, which leads to the degradation of the mesoporous network and formation of interconnected pore channels. In general, POSS appears to increase the concentration of pores between 4–10 nm.

The pore volumes and specific surface areas after HF etching are shown in Fig. 6 as determined by the NLDFT theory. For the samples with Fe, the pore volume increases between 1100 °C and 1300 °C and is relatively constant from 1300 °C to 1500 °C. However, the specific surface area significantly decreases from 1300 °C to 1500 °C while remaining relatively constant from 1100 °C to 1300 °C. This phenomenon is also correlated to the formation of aggregated SiO_2 networks and domains that are removed after HF etching. For the *x*POSS–0Fe samples, the pore volume and specific surface area all increase with temperature. In general, the pore volume of the *x*POSS–1Fe samples remains relatively constant between 0.35–0.4 cm^3 g^{-1} between 1100 °C and 1500 °C, while the specific surface area decreases prominently between 1300 °C and 1500 °C from ~600 m^2 g^{-1} to ~250 m^2 g^{-1}. In the *x*POSS–0Fe samples, the pore size generally increases from ~0.02 cm^3 g^{-1} at 1100 °C, to ~0.12–0.3 cm^3 g^{-1} at 1300 °C, and to ~0.35 cm^3 g^{-1} at 1500 °C. Similarly, the specific surface area increases from ~40 m^2 g^{-1}, to ~300–600 m^2 g^{-1}, and to ~700 m^2 g^{-1} at 1100 °C, 1300 °C, and 1500 °C, respectively. Notably, there is a much larger spread in pore volume and specific surface area values as a function of the POSS content in the

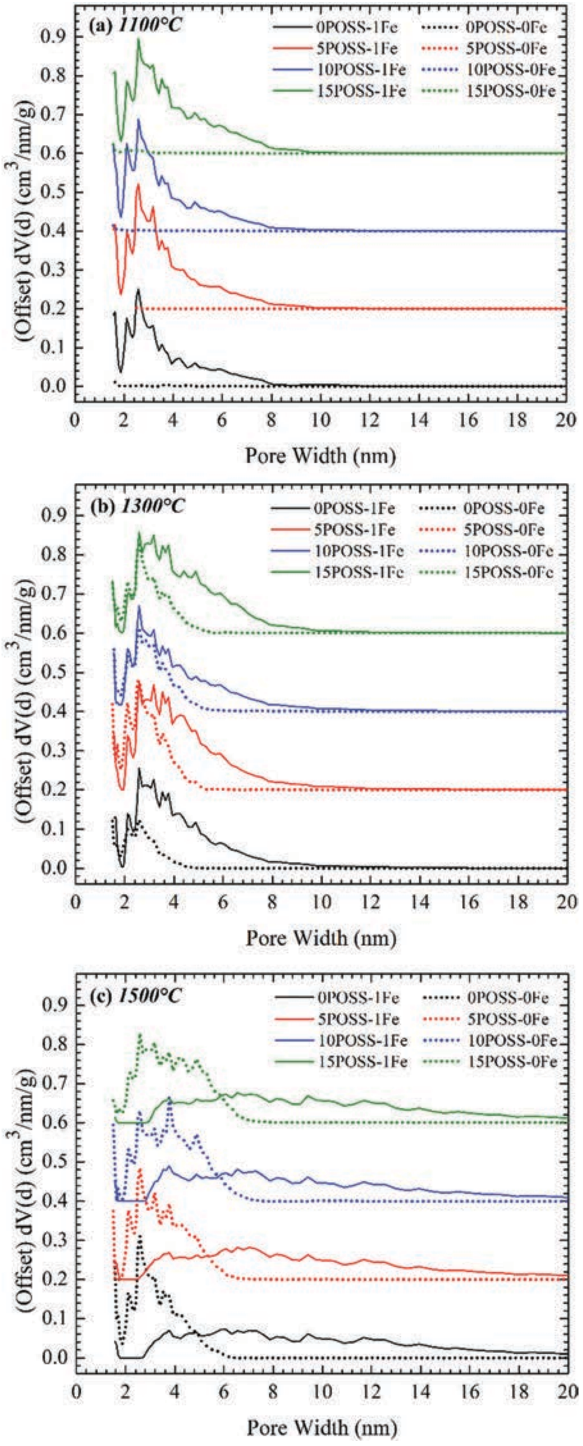

Fig. 5 Pore size distributions of HF-etched 0% (black), 5% (blue), 10% (red), and 15% (green) POSS samples with Fe (solid line) and without Fe (dotted line) at (a) 1100 °C, (b) 1300 °C, and (c) 1500 °C calculated from NLDFT theory. Distributions are offset for clarity.

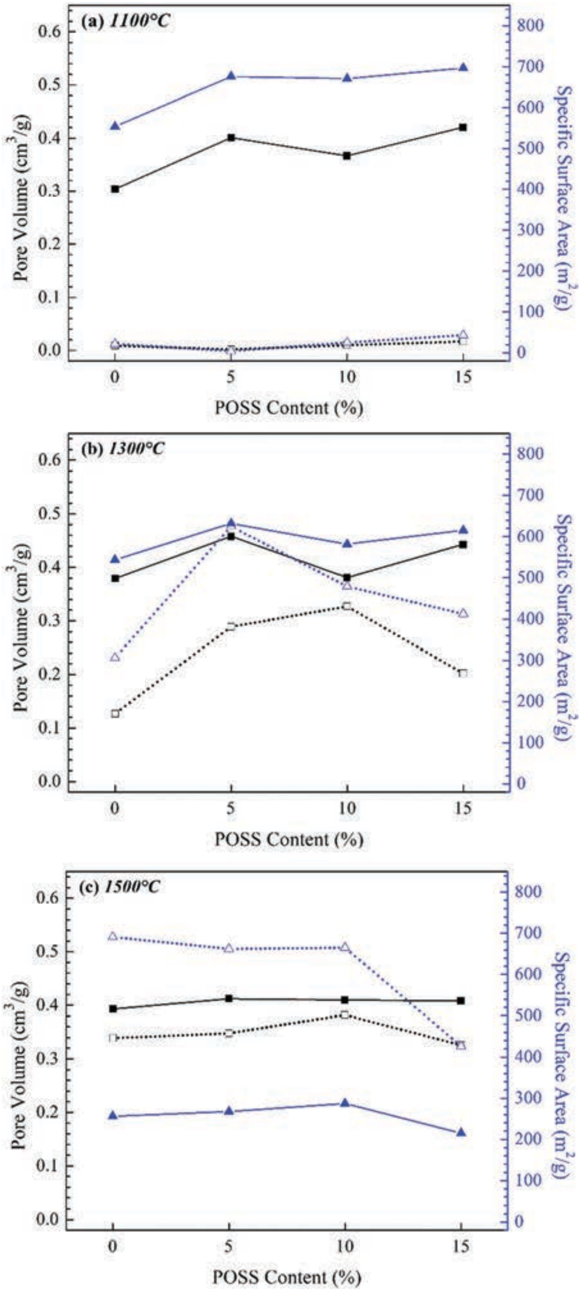

Fig. 6 Pore volume (black) and specific surface area (blue) of HF-etched samples with Fe (solid line) and without Fe (dotted line) at (a) 1100 °C, (b) 1300 °C, and (c) 1500 °C as a function of POSS content.

*x*POSS–0Fe samples at 1300 °C compared to the *x*POSS–1Fe samples. This can be attributed to the initial stages of SiO_2 phase separation from the amorphous SiOC matrix and agglomeration of POSS-derived SiO_2 nanodomains. At 1500 °C, the *x*POSS–0Fe samples generally have consistent pore volume and surface area values across the POSS values as the phase separated SiO_2 domains are more refined. POSS-derived SiO_2 nanodomain agglomeration at the 15POSS–0Fe condition could account for the observed decrease in specific surface area.

With the addition of POSS, the pore volume and specific surface area both increase. There is minimal change between 5% and 10% POSS concentrations for the Fe-containing samples and a decrease at 1300 °C due to the aforementioned aggregation of the SiO_2 nanodomains prior to HF-etching. POSS content and temperature therefore have competing effects on pore characteristics, specifically in regard to the formation and distribution of

SiO_2 nanodomains. At higher temperature and higher POSS content, SiO_2 nanodomains generated from POSS serve as the nucleation sites for the growth of the amorphous SiO_2 domains. However, these sites appear to lose coherency and begin aggregating at 10% POSS content, which contributes to the formation of pores between 5 and 10 nm per Fig. 5(a–c) between 1100 °C and 1300 °C. In the samples without Fe, SiO_2 nanodomain formation in the absence of POSS only appreciably occurs above 1300 °C, which explains why the sorption curves of Fig. 5(c) show H4-type hysteresis instead of H2-type hysteresis as the interconnected pore network has yet to materialize.

3.4 Thermodynamic modelling

A computational model can be established to predict the relative phase content and understand the catalytic role of Fe in β-SiC nucleation and amorphous SiO_xC_y phase separation. Thermodynamic modeling of pure SiOC based on Gibbs free energy minimization has been performed in earlier work[59,66] as well as in an analogous Si–C–N system.[67] In the current work, the catalytic generation of β-SiC by Fe is introduced. The goal of this model is to estimate the phase profile given the overall sample composition and the core thermodynamic phenomena. However, it should be noted that this model only considers phases between 1100 °C and 1500 °C pyrolysis temperatures and low Fe content (less than 5 mol%) as a higher Fe content would yield ancillary reactions and ferrous phase formation that requires more dedicated investigation into the relative reaction kinetics. Furthermore, this restriction keeps in line with the treatment of Fe as a catalyst that does not appreciably contribute to the phase profile of the pyrolyzed ceramics. In addition, this model assumes that the system is sufficiently carbon-rich so Fe_xSi_y formation occurs *via* consumption of Fe_3C rather than FeO_x derivatives.

A sample with an overall composition of $SiFe_\alpha O_\beta C_\delta$ may be first treated as nominally-single phase, which then undergoes phase separation to yield Fe_3Si/Fe_5Si_3, C, SiC, SiO_2, and SiO_xC_y phases. Fig. 7 gives schematic Si–Fe–O–C phase diagrams that show the bounds for the $SiFe_\alpha O_\beta C_\delta$ system such that Fe_3Si (Fig. 7(a)) or Fe_5Si_3 (Fig. 7(b)) exists in equilibrium with SiC, SiO_2, SiO_xC_y, and free C phases. In either case, phase separation is modeled to proceed from the nominally-single phase $SiFe_\alpha O_\beta C_\delta$ to Fe_uSi_v and amorphous SiO_aC_b. SiO_aC_b further separates to free C and amorphous SiO_xC_y, here represented without excess C. Of note on the Si–O–C plane, the SiO_aC_b system is bounded by region C–SiO_2–SiC, and SiO_xC_y exists on the tie-line between SiC and SiO_2. This final amorphous SiO_xC_y phase is the combination of SiC, SiO_2, and intermediate $SiO_{(4-i)/2}C_{i/4}$ (for i = 1 to 3) phases along the SiC–SiO_2 tie-line. The relative amounts of each $SiO_{(4-i)/2}C_{i/4}$ phase along with SiC and SiO_2 are temperature-dependent.

The overall segregation reaction can be expressed as

$$SiFe_\alpha O_\beta C_\delta \Rightarrow f_M Fe_3Si + f_C C_{free} + (1 - f_M - f_C)SiO_xC_y \quad (10)$$

in which f_M and f_C refer to the fractions of the Fe_3Si and free C phases, respectively. For simplicity, only Fe_3Si is considered in the following derivation as the procedure is similar for Fe_5Si_3 and the phase fraction is expected to be quite low for either silicide. Since Si and O compositions along the C–SiO_xC_y tie-line are constant, it is evident that the O coefficient on either side of eqn (10) is the same:

$$\beta = x \quad (11)$$

As SiO_xC_y can be expressed as $SiO_{(4-i)/2}C_{i/4}$ to satisfy the stoichiometric constraints imposed on the SiC–SiO_2 tie-line, then the relationship between x and y can be identified as:

$$y = \frac{4 - 2x}{4} = \frac{4 - 2\beta}{4} \quad (12)$$

Therefore, the free C phase fraction is the stoichiometric difference between C in the SiO_xC_y and the nominal $SiFe_\alpha O_\beta C_\delta$ phases:

$$f_C = \frac{\delta - y}{1 + \alpha + \beta + \delta} = \frac{\delta - \frac{4 - 2\beta}{4}}{1 + \alpha + \beta + \delta} = \frac{0.5\beta + \delta - 1}{1 + \alpha + \beta + \delta} \quad (13)$$

Due to the restraint that only the Fe_3Si phase forms, then the

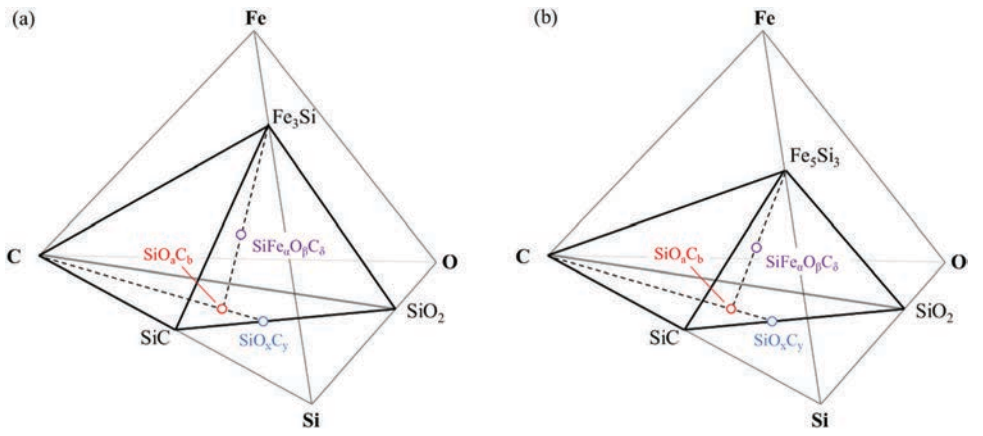

Fig. 7 Schematic phase diagrams of Si–Fe–O–C quaternary system and phase separation of a nominal $SiFe_\alpha O_\beta C_\delta$ into (a) Fe_3Si, C, SiC, SiO_2, and SiO_xC_y (1100–1300 °C) or (b) Fe_5Si_3, C, SiO_2, SiC, and SiO_xC_y (1300–1500 °C).

phase fraction of Fe_3Si is

$$f_{\mathrm{M}} = \frac{\frac{1}{3}\alpha}{1 + \alpha + \beta + \delta} \tag{14}$$

The final phase separation event is SiO_xC_y along the SiO_2–SiC tie-line into a combination of SiO_2, SiC, and intermediate $SiO_{(4-i)/2}C_{i/4}$ (for i = 1 to 3) phases, in which f_0, f_1, f_2, f_3, and f_4 refer to phase fractions of SiO_2, $SiO_{3/2}C_{1/4}$, $SiOC_{1/2}$, $SiO_{1/2}C_{3/4}$, and SiC, respectively:

$$\mathrm{SiO}_x\mathrm{C}_y \Rightarrow f_0\mathrm{SiO}_2 + f_1\mathrm{SiO}_{\frac{3}{2}}\mathrm{C}_{\frac{1}{4}} + f_2\mathrm{SiOC}_{\frac{1}{2}} + f_3\mathrm{SiO}_{\frac{1}{2}}\mathrm{C}_{\frac{3}{4}} + f_4\mathrm{SiC} \tag{15}$$

whereas the phase fractions of Fe_3Si and free C are largely based on stoichiometric coefficients, the relative phase fractions of the five Si–O–C phases are codependent and should represent the most stable configuration based on the pyrolytic temperature. This configuration is related to the minimized Gibbs free energy of the total phase-separated amorphous system, represented as:

$$G_{\mathrm{total}} = \sum_i [f_i(T) \times G_i(T) + RT(f_i(T) \times \ln(f_i(T)))] \tag{16}$$

in which $G_i(T)$ is the Gibbs free energy of amorphous phase i (for i = 0 to 4) as a function of temperature. The Gibbs free energy of amorphous SiC and SiO_2 is taken from available data[59,67,68] for the crystalline analogs and the vitrification energy, ΔE, to account for the loss of crystallinity:

$$G^{\mathrm{am}}(T) = G^{\mathrm{cr}}(T) + \Delta E \tag{17}$$

In order to account for the varied stoichiometries, a normalization factor n_{Form} equal to the number of atoms in the formula (*e.g.*, $n_{\mathrm{Form}}(SiO_2) = 3$, $n_{\mathrm{Form}}(SiC) = 2$, *etc.*) is introduced, per an earlier analogous study.[67] In maintaining with prior convention, all Gibbs energies are expressed with units $[\mathrm{kJ\ M_{fu}}^{-1}]$ obtained by G_i/n_{Form}. Then for ΔE of 54 and 6.9 kJ mol^{-1} for SiC and SiO_2, respectively,[59] the Gibbs free energies of amorphous SiO_2 and SiC as a function of temperature are

$$G^{\mathrm{am}}_{\mathrm{SiO_2}}(T) = G^{\mathrm{am}}_0(T) = G^{\mathrm{cr}}_{\mathrm{SiO_2}}(T) + 2.3\ [\mathrm{kJ\ M_{fu}}^{-1}] \tag{18}$$

$$G^{\mathrm{am}}_{\mathrm{SiC}}(T) = G^{\mathrm{am}}_4(T) = G^{\mathrm{cr}}_{\mathrm{SiC}}(T) + 27\ [\mathrm{kJ\ M_{fu}}^{-1}] \tag{19}$$

The Gibbs free energies of the intermediate amorphous SiO_xC_y phases are calculated as the summation of the number of constituting Si–O or Si–C bonds assuming a tetrahedral structure in the amorphous matrix and the energies of the constituting Si–O or Si–C bonds. These bond energies are approximated as a quarter of the total bonds about a Si atom in one tetrahedral unit of the respective crystalline form:

$$G^{\mathrm{am}}_{\mathrm{SiO_{\frac{3}{2}}C_{\frac{1}{4}}}}(T) = G^{\mathrm{am}}_1(T) = \frac{1}{4}G^{\mathrm{am}}_{\mathrm{SiC}}(T) + \frac{3}{4}G^{\mathrm{am}}_{\mathrm{SiO_2}}(T) \tag{20}$$

$$G^{\mathrm{am}}_{\mathrm{SiOC_{\frac{1}{2}}}}(T) = G^{\mathrm{am}}_2(T) = \frac{1}{2}G^{\mathrm{am}}_{\mathrm{SiC}}(T) + \frac{1}{2}G^{\mathrm{am}}_{\mathrm{SiO_2}}(T) \tag{21}$$

$$G^{\mathrm{am}}_{\mathrm{SiO_{\frac{1}{2}}C_{\frac{3}{4}}}}(T) = G^{\mathrm{am}}_3(T) = \frac{3}{4}G^{\mathrm{am}}_{\mathrm{SiC}}(T) + \frac{1}{4}G^{\mathrm{am}}_{\mathrm{SiO_2}}(T) \tag{22}$$

The catalytic effect of Fe locally reduces the energetic barrier to β-SiC nucleation. In other Si–Fe–O–C systems, SiC nanowire growth has been observed with a Fe–Si droplet at the tip of the nanowire.[69–76] Fe was similarly observed to catalyze both HfC[77] and Si_3N_4[78] nanowire formation with the presence of a Fe-rich droplet at the tip of each nanowire, which furthers the notion that an intermediate ferrous alloy generated in the matrix catalyzes metal carbide nucleation through the vapor–liquid–solid (VLS) mechanism. In other studies, energy dispersive X-ray spectroscopy (EDS) confirmed that the droplet at the tip of SiC nanowires was primarily comprised of Fe and Si.[72–74] However, in studies of Fe-catalyzed SiC nanowire growth, the nanowires were free to grow from a substrate – generally in chemical vapor deposition experiments[71] or porous media[69,73] – and were not restricted by a solid matrix. As solid-state diffusion is slow and especially limited in the pyrolyzed SiFeOC ceramic samples, nanowire growth is neither expected nor observed in this study. This treatment assumes the β-SiC growth is from the very initial stages of VLS/SLS nanowire growth, but is restricted by both the dense microstructure and high solid-state diffusional barriers. Classical nucleation and VLS/SLS growth theories can be approximated and adapted to model the SiC formation.

In the carbon-rich SiOC matrix, Fe_3C nominally exists at ~700 °C prior to conversion to Fe_3Si. In addition, Fe_3C was not observed in XRD spectra in a previous study[38] and EDS performed on Fe alloy droplets found on SiC nanowires only showed Fe and Si, as mentioned earlier. Therefore, the VLS mechanism most likely proceeds through a liquid Fe–C–Si alloy that quenches to Fe_3Si per eqn (5) after available reactants are consumed. The gaseous precursors for the VLS mechanism would be SiO and/or CO evolved from the reaction of SiO_2 and C in eqn (2) and (3). SiO and CO diffuse into the Fe–C–Si alloy droplet – denoted as $[\mathrm{Fe{-}Si{-}C}]_{\mathrm{droplet}}$ – leading to supersaturation of Si and C in the droplet.

$$\mathrm{SiO} + 3\mathrm{CO} + \{\mathrm{Fe{-}Si{-}C}\}_{\mathrm{droplet}} \rightarrow \{\mathrm{Fe{-}2Si{-}2C}\}_{\mathrm{droplet}} + 2\mathrm{CO_2} \tag{23}$$

SiC precipitation is then driven by the supersaturation of Si and C in the droplet.

$$\{\mathrm{Fe{-}2Si{-}2C}\}_{\mathrm{droplet}} \rightarrow \{\mathrm{Fe{-}Si{-}C}\}_{\mathrm{droplet}} + \mathrm{SiC}(\beta) \tag{24}$$

It is also possible that some SiC is formed from the reduction of evolved SiO with C from eqn (4), and more CO is evolved from the reaction between CO_2 and C

$$\mathrm{C} + \mathrm{CO_2} \rightarrow 2\mathrm{CO} \tag{25}$$

This CO evolution also explains in part the origin to the ceramic yield discrepancies between Fe-containing and Fe-free samples. The corresponding SLS contribution could account for the enhanced phase separation of the amorphous Si–O–C matrix to yield SiO_2 and β-SiC. It is postulated that free C diffusion into the Fe_xSi_y droplet is more likely than SiO_xC_y diffusion due to the inherent stability of the amorphous ceramic. Sufficient C supersaturation is then thought to yield β-SiC, with the remnant Fe–C droplet quenching to Fe_3Si per eqn (5) when the available reactants are depleted. However, dedicated atomistic modeling would be required to confirm or verify this process and what is presented is merely a potential mechanism. In practicality, the catalytic process is a hybrid of VLS and SLS mechanisms, with SLS believed to occur at lower temperatures in the dense microstructure and VLS occurring at higher temperatures as internal pores form due to gas evolution and transport.

From classical nucleation theory, the steady-state nucleation rate (J_0) increases as energetic requirement for nucleation (ΔG_{Nucl}) decreases,

$$J_0 = A\mathrm{e}^{-\frac{\Delta G_{\mathrm{Nucl}}}{k_{\mathrm{B}}T}} \tag{26}$$

in which A is a pre-exponential factor, k_{B} is Boltzmann's constant, and T is absolute temperature. The critical energy barrier can be further expressed as:

$$\Delta G_{\mathrm{Nucl}} = \frac{16\pi{\gamma_{\mathrm{LV}}}^3}{3(\Delta G_{\mathrm{v}})^2}\frac{2 - 3\cos\theta + \cos^3\theta}{4} \tag{27}$$

with γ_{LV} the interfacial surface energy between the liquid catalyst droplet and the precursor vapor/solid phase, θ the contact angle between the deposited solid phase and liquid catalyst droplet, and ΔG_{v} the Gibbs free energy change per unit volume of the solid phase. ΔG_{v} can be further defined as:

$$\Delta G_{\mathrm{v}} = -\frac{k_{\mathrm{b}}T}{\Omega\ln(1+\sigma)} \tag{28}$$

in which Ω is the molar volume, and σ the degree of supersaturation. Due to the lack of available data regarding solid–solid interfacial energies of Si–O–C derivatives and the thermodynamic complexity of the ternary Fe–Si–C liquid catalyst, several approximations are made to estimate the energetic contribution of VLS/SLS-mediated SiC formation, specifically that of the interfacial energy and supersaturation. A contact angle of 135° is assumed based on previous studies that investigated the wettability and interfacial energy of Cu and Ni on SiC[79] and microstructures of Fe_xSi_y-capped SiC nanowires. In the aforementioned system, Sn and Ni droplets were also studied on SiC with interfacial energies between 1.5 to 3.0 J m^{-2}. When computed for the SiC–liquid interface, the interfacial energy between the liquid droplet precursor vapor/solid phase is approximated as 1 J m^{-2}, as it is difficult to differentiate the prevailing growth mechanism. Furthermore, the surface energies of Au nanoparticles (<10 nm) were computationally modeled and reported between 0.5 and 1 J m^{-2},[80] so such an approximation may be accepted for this nanoscale system.

While supersaturation is usually presented as the ratio of excess solute concentration to the equilibrium concentration, the complexity of simultaneous C and Si supersaturation in the alloy droplet (needed to nucleate SiC per the Fe–C–Si phase diagram near the liquidus temperature[81]) cannot be reasonably derived in available thermodynamic and kinetic models. For VLS nanowire systems, an estimated supersaturation has been postulated with regards to the critical nanowire (d_{cr}) and as-grown nanowire (d_{NW}) diameter:[82]

$$\sigma \approx 2\frac{\Omega_{\mathrm{at}}\gamma_{\mathrm{SL}}}{k_{\mathrm{B}}T}\left[\frac{1}{d_{\mathrm{cr}}} - \frac{1}{d_{\mathrm{NW}}}\right] \tag{29}$$

in which Ω_{at} is the atomic volume of the nanowire and γ_{SL} is the interfacial energy between the nanowire and the liquid droplet. Similarly, for the nanoparticle system, γ_{SL} is assumed as 1 J m^{-2}. Based on the crystallite size in Table 1 between 1100 °C and 1300 °C for the 0POSS–0Fe samples, the β-SiC nuclei that form intrinsically from phase separation can be roughly correlated as the critical size. In the 0POSS–1Fe condition, β-SiC nucleation has initiated at 1100 °C with crystallite sizes of ∼5 nm, which indicates that the critical barrier has been surpassed at the initial stages of quasi-nanowire growth. For this analysis, the critical nuclei and observed nanoparticle sizes are roughly approximated as $d_{\mathrm{cr}} \approx 2$ nm (all temperatures) and $d = d_{\mathrm{NW}} \approx$ 5 nm (1100 °C) or 7 nm (1300–1500 °C), respectively. However, in actuality the size may be lower but cannot be verified due to instrument detection limits. Further nanostructure or atomistic modeling studies can be performed to refine these values, but are accepted with the intention of providing baseline model parameters. Then, the Gibbs free energy of the SiC phase is the combined contributions from SiC formed by phase separation and nucleation factors from eqn (21) and (27)–(29):

$$G_4'(T) = G_4^{\mathrm{cr}}(T) - n_{\mathrm{Nucl}}\Delta G_{\mathrm{Nucl}} \tag{30}$$

in which n_{Nucl} is a normalization factor to account for the molar ratio of Fe and the atomic units in stoichiometric $SiFe_{\alpha}O_{\beta}C_{y}$ for the aforementioned unit convention.

$$\begin{aligned} n_{\mathrm{Nucl}} &= \frac{\alpha}{1+\alpha+\beta+\delta}\left(\frac{1}{1+\alpha+\beta+y}\right) \\ &= \frac{\alpha}{1+\alpha+\beta+\delta}\left(\frac{1}{2+\alpha+0.5\beta}\right) \end{aligned} \tag{31}$$

Here, MATLAB has been used to perform the Gibbs energy minimization calculation (see S4, ESI†), and the predicted phase fractions based on the sample composition from elemental analysis (*e.g.*, ICP-OES, carbon combustion) for 0POSS–0Fe and 0POSS–1Fe samples at 1100, 1300, and 1500 °C are presented in Table 3 (E.A. (calc.)). In addition, the predicted phase fractions were generated from the calculated sample compositions from NMR analysis in Table 2 (NMR (calc.)). As neither Fe_3Si nor Fe_5Si_3 could be observed in the NMR spectra, the Fe content from the corresponding elemental analysis is used to generate the expected phase content. The corresponding phase fractions obtained from NMR peak fitting analysis (Table 2) are also presented for comparison (NMR (peak fit)). For the 0POSS–0Fe_1100 sample, the phase content from elemental analysis could not be calculated by this model due to an abnormally high O coefficient, which will be discussed later. The calculated phase content from both E.A. and NMR agree fairly closely with the phase fractions obtained from NMR peak fitting for the 0POSS–1Fe_1100 sample.

Table 3 Predicted phase content of SiO_xC_y species for 0POSS–0Fe and 0POSS–1Fe samples at 1100, 1300, and 1500 °C calculated from Gibbs energy minimization performed in MATLAB. Calculated phase content is given for compositions obtained from elemental analysis (E.A.) and NMR. The phase content obtained from NMR peak fitting (Table 2) is provided for reference

			Phase content of SiO_xC_y species (%)				
Sample	Composition		SiO_2	$SiO_{3/2}C_{1/4}$	$SiOC_{1/2}$	$SiO_{1/2}C_{3/4}$	SiC
0POSS–0Fe_1100	$SiO_{2.405\pm0.003}C_{3.259\pm0.004}$	E.A. (calc.)	—	—	—	—	—
	$SiO_{1.20}C_{0.40}$	NMR (calc.)	39.1	19.6	9.9	5.0	26.5
		NMR (peak fit)	*25*	*22.5*	*30.3*	*12.3*	*9.8*
0POSS–1Fe_1100	$SiO_{1.483\pm0.002}C_{4.924\pm0.006}$ ($Fe_{0.013}$)	E.A. (calc.)	54.0	26.7	7.9	3.0	14.5
	$SiO_{1.44}C_{0.28}$	NMR (calc.)	52.8	19.8	7.4	2.8	17.3
		NMR (peak fit)	*56.6*	*13.3*	*8.7*	*5.4*	*16.1*
0POSS–0Fe_1300	$SiO_{1.457\pm0.001}C_{4.489\ \pm\ 0.003}$	E.A. (calc.)	50.7	21.9	9.5	4.1	13.9
	$SiO_{1.30}C_{0.33}$	NMR (calc.)	42.6	21.2	10.5	5.2	20.5
		NMR (peak fit)	*60*	*6.3*	*0.5*	*5.5*	*28.2*
0POSS–1Fe_1300	$SiO_{1.313\pm0.001}C_{4.436\pm0.002}$ ($Fe_{0.016}$)	E.A. (calc.)	43.9	20.9	9.9	4.7	20.7
	$SiO_{0.90}C_{0.52}$	NMR (calc.)	26.9	15.9	9.4	5.6	42.1
		NMR (peak fit)	*43.7*	*0.5*	*0.5*	*8.5*	*46.9*
0POSS–0Fe_1500	$SiO_{1.133\pm0.002}C_{4.439\pm0.006}$	E.A. (calc.)	33.7	20.2	12.1	7.2	26.9
	$SiO_{0.35}C_{0.79}$	NMR (calc.)	5.9	6.9	8.1	9.5	69.6
		NMR (peak fit)	*13.3*	*0.7*	*3.6*	*9.3*	*73.1*
0POSS–1Fe_1500	$SiO_{0.485\pm0.001}C_{3.310\pm0.001}$ ($Fe_{0.019}$)	E.A. (calc.)	10.2	9.7	9.2	8.7	62.2
	$SiO_{0.21}C_{0.85}$	NMR (calc.)	3.2	4.1	5.2	6.6	81.0
		NMR (peak fit)	*0.8*	*2.1*	*10.6*	*14.1*	*72.4*

In general, the phase profiles calculated from the NMR composition and observed *via* NMR peak fitting agree and follow expected trends. However, there is some difference in the expected SiO_2 and $SiO_{3/2}C_{1/4}$ contents between the two NMR values, with peak fitting giving higher SiO_2 and lower $SiO_{3/2}C_{1/4}$ phase fractions than the calculated values. In these cases (specifically the 0POSS–0Fe_1300, 0POSS–1Fe_1300, and 0POSS–0Fe_1500 samples), it is interesting that the sum of the two phases from the calculated profile approximately equals that from the peak fit profile (*e.g.*, for 0POSS–1Fe_1300 sample, SiO_2 (42.6%) + $SiO_{3/2}C_{1/4}$ (21.2%) ≈ SiO_2 (60.0%) + $SiO_{3/2}C_{1/4}$ (6.3%)). This indicates there is some intrinsic SiO_xC_y phase separation occurring in this regime, which can be implemented in future models upon study. The NMR peaks for SiO_2 (~-107 ppm) and $SiO_{3/2}C_{1/4}$ (~-64 ppm) are reasonably distinct so it is not believed that peak deconvolution issues significantly cause this discrepancy. The phase content variations for the intermediate SiO_xC_y phases increase with temperature, and this may be attributed to detection limitations and high background noise present in the NMR spectra.

While the overall phase content trends generally agree in Table 3, the difference between the NMR calculated and peak fitting phase contents for the 0POSS–0Fe_1100 sample is quite large and starkly different than the other samples. For the phase fractions calculated in Table 3, the Gibbs energy minimization program used reference values for amorphous SiO_2 $\left(G^{\mathrm{am}}_{\mathrm{SiO_2}}(T)\right)$ and crystalline SiC ($G^{\mathrm{cr}}_{\mathrm{SiC}}(T)$), which are the prevailing phases in this temperature range. Per the XRD spectrum in Fig. 1(a), the 0POSS–0Fe_1100 sample is generally amorphous, so these assumptions may not truly apply. The phase content was recalculated using reference amorphous SiO_2 $\left(G^{\mathrm{am}}_{\mathrm{SiO_2}}(T)\right)$ and SiC ($G^{\mathrm{am}}_{\mathrm{SiC}}(T)$) and presented in Table 4. As a result, the phase profile more closely matches the NMR peak fitting profile but has slight deviations for the SiO_xC_y phases. Further model development is needed to determine the transition point between the applicability of either amorphous or crystalline SiC Gibbs energy reference values, but can be assumed that below 1100 °C the amorphous value better represents the SiOC system.

Although the initial results are promising, the discrepancies between NMR and elemental analysis compositions preclude a true direct comparison. Due to the low concentration, Fe_xSi_y content could not be discerned due to high signal-to-noise ratios. In this vein, low concentrations of any SiO_xC_y clusters may not be discernable or correctly modeled with the peak fitting algorithm. Significant peak broadening due to the nanodomain SiO_xC_y clusters can also mitigate proper peak fitting results. As Si NMR detects unique bonding environments, this might not directly correlate to truly realized or refined phases. Rather, the bonding environments in the amorphous structure most likely are a few nanometers of the Si atom size. Furthermore, the C and Si contents in Table 3 are measured using different techniques (ICP-OES and carbon combustion). Overall, Table 3 shows that the calculated phase fractions for SiC are lower than those from the NMR characterization. In all the samples except for 0POSS–1Fe_110C, the O coefficient is larger than that obtained from NMR peak fitting, with the discrepancy increasing with temperature. In this model, a higher O coefficient yields more SiO_2 content generally at the expense of SiC. As the O coefficient was calculated as the residual assuming 100% of Si, Fe, O, and C values, this corresponds to the Si amount from ICP being reported lower than expected (assuming the C values from the combustion method are accurate). While the solutions were analyzed by ICP on the same day as preparation, it is believed that some amount of SiO_2 can polymerize and precipitate from the digestion solution even when CsCl and H_3BO_3 are used as ionization and SiO_2 stabilization compounds, respectively. For the 0POSS–0Fe_1100 sample, this is believed to inhibit similar phase prediction from the E.A. composition. In addition, this intrinsic issue causes the

Table 4 Predicted phase content of SiO_xC_y species for 0POSS–0Fe_1100 using reference $G^{am}_{SiO_2}(T)$ and $G^{am}_{SiC}(T)$ values in the Gibbs energy minimization model. Phase contents calculated using reference $G^{am}_{SiO_2}(T)$ and $G^{cr}_{SiC}(T)$ values (Table 3) and from NMR peak fitting (Table 2) are provided as reference

			Phase content of SiO_xC_y species (%)				
Sample	Composition	Reference values	SiO_2	$SiO_{3/2}C_{1/4}$	$SiOC_{1/2}$	$SiO_{1/2}C_{3/4}$	SiC
0POSS–0Fe_1100	$SiO_{1.20}C_{0.40}$	SiO_2(am)–SiC(am)	28.8	23.5	19.2	15.7	12.8
		SiO_2(am)–SiC(cr)	39.1	19.6	9.9	5	26.5
		NMR (peak fit)	25	22.5	30.3	12.3	9.8

expected SiC content in the 0POSS–0Fe_1300, 0POSS–1Fe_1300, and 0POSS–0Fe_1500 samples to be far smaller than those from both NMR profiles. To further improve this method, there is a need for thermodynamic model refinement, accurate data input regarding solid–solid interfacial energies of Si–O–C derivatives, and thorough understanding of the thermodynamic complexity of the Fe–Si–C liquid catalyst. More importantly, accurate elemental composition analysis is a must, which is our ongoing effort. Dedicated atomistic modeling can also yield insight into both model parameters and mechanistic pathways for VLS/SLS-driven SiC formation. Overall, the Gibbs free energy model reliably predicts phase content in regards to observed trends from XRD and NMR across the studied temperatures, while presenting a more comprehensive, affordable, and fast method of calculating phase fractions of different amorphous SiOC clusters and evaluating the catalytic effect of active fillers in driving phase formation.

4. Conclusions

The effects of Fe and POSS on the phase formation of SiOC between 1100 °C and 1500 °C were studied. At 1100 °C, Fe is sufficient to catalyze nucleation and growth of the SiC phase, which provides energetically favorable nucleation sites for further SiC growth at higher pyrolytic temperatures. At all temperatures, the SiC phase is more prevalent in the Fe-containing samples. In addition to reported SiC nucleation and graphitization, Fe induces phase separation of the amorphous SiOC phase, which yields a higher SiO_2 content. Specific surface areas of etched Fe-containing samples are between 600–700 $m^2\ g^{-1}$ from 1100 °C to 1300 °C, but decrease to between 200 and 300 $m^2\ g^{-1}$ at 1500 °C due to the growth and coalescence of the segregated SiO_2 phase. At 1100 °C and 1300 °C, the specific surface areas of the samples with Fe are larger than those of the samples without Fe. Phase contents of the 1100, 1300, and 1500 °C pyrolyzed samples are calculated based on a modified Gibbs free energy minimization method which utilizes a modified VLS/SLS mechanism to explain the role of Fe in catalyzation of SiC formation.

Author contributions

Advaith V. Rau: conceptualization, data curation, formal analysis, investigation, methodology, software, validation, visualization, writing – original draft. Ken Knott Jr.: investigation, resources, validation. Kathy Lu: conceptualization, funding acquisition, project administration, resources, supervision, validation, writing – review & editing.

Conflicts of interest

The authors declare that they have no known competing financial interests or personal relationships that could have appeared to influence the work reported in this paper.

Acknowledgements

This work was supported by the National Science Foundation under the grant no. CBET-2024546.

References

1 K. Lu, Porous and high surface area silicon oxycarbide-based materials—A review, *Mater. Sci. Eng., R*, 2015, **97**, 23–49.

2 P. Greil, Polymer derived engineering ceramics, *Adv. Eng. Mater.*, 2000, **2**(6), 339–348.

3 P. Colombo, G. Mera, R. Riedel and G. D. Sorarù, Polymer-derived ceramics: 40 years of research and innovation in advanced ceramics, *J. Am. Ceram. Soc.*, 2010, **93**, 1805–1837.

4 K. Lu and D. Erb, Polymer derived silicon oxycarbide-based coatings, *Int. Mater. Rev.*, 2017, **63**(3), 139–161.

5 C. Vakifahmetoglu, D. Zeydanli and P. Colombo, Porous polymer derived ceramics, *Mater. Sci. Eng., R*, 2016, **106**, 1–30.

6 A. Strachota, M. Černý, Z. Chlup, K. Rodzeń, K. Depa, M. Halasová, M. Šlouf and J. Schweigstillová, Preparation of finely macroporous SiOC foams with high mechanical properties and with hierarchical porosity *via* pyrolysis of a siloxane/epoxide composite, *Ceram. Int.*, 2015, **41**(7), 8402–8410.

7 X. Yan, D. Su and S. Han, Phase separation induced macroporous SiOC ceramics derived from polysiloxane, *J. Eur. Ceram. Soc.*, 2015, **35**(2), 443–450.

8 Y. Blum, G. D. Sorarù, A. P. Ramaswamy, D. Hui, S. M. Carturan and R. Riedel, Controlled mesoporosity in SiOC *via* chemically bonded polymeric spacers, *J. Am. Ceram. Soc.*, 2013, **96**(9), 2785–2792.

9 Z. Yu, Y. Feng, S. Li and Y. Pei, Influence of the polymer–polymer miscibility on the formation of mesoporous SiC(O) ceramics for highly efficient adsorption of organic dyes, *J. Eur. Ceram. Soc.*, 2016, **36**(15), 3627–3635.

10 P. Jana, M. C. Bruzzoniti, M. Appendini, L. Rivoira, M. Del Bubba, D. Rossini, L. Ciofi and G. D. Sorarù, Processing of polymer-derived silicon carbide foams and their adsorption capacity for non-steroidal anti-inflammatory drugs, *Ceram. Int.*, 2016, **42**(16), 18937–18943.

11 P. Jana, E. Zera and G. D. Sorarù, Processing of preceramic polymer to low density silicon carbide foam, *Mater. Des.*, 2017, **116**, 278–286.

12 D. Erb and K. Lu, Effect of additive structure and size on SiO_2 formation in polymer-derived SiOC ceramics, *J. Am. Ceram. Soc.*, 2018, **101**(12), 5378–5388.

13 D. Erb and K. Lu, Additive and pyrolysis atmosphere effects on polysiloxane-derived porous SiOC ceramics, *J. Eur. Ceram. Soc.*, 2017, **37**(15), 4547–4557.

14 J. Li, K. Lu, T. Lin, F. Shen and P. Colombo, Preparation of micro-/mesoporous SiOC bulk ceramics, *J. Am. Ceram. Soc.*, 2015, **98**(6), 1753–1761.

15 J. Li, K. Lu and R. Riedel, Highly porous SiOC bulk ceramics with water vapor assisted pyrolysis, *J. Am. Ceram. Soc.*, 2015, **98**(8), 2357–2365.

16 R. Pena-Alonso, G. D. Soraru and R. Raj, Preparation of ultrathin-walled carbon-based nanoporous structures by etching pseudo-amorphous silicon oxycarbide ceramics, *J. Am. Ceram. Soc.*, 2006, **89**(8), 2473–2480.

17 P. Colombo, Engineering porosity in polymer-derived ceramics, *J. Eur. Ceram. Soc.*, 2008, **28**(7), 1389–1395.

18 P. S. Liu and G. F. Chen, General introduction to porous materials, in *Porous Materials: Processing and Applications*, Butterworth-Heinemann, 2014, ch. 1pp. 1–20.

19 T. Rouxel, G. Massouras and G. D. Soraru, High temperature behavior of a gel-derived SiOC glass: Elasticity and viscosity, *J. Sol–Gel Sci. Technol.*, 1999, **14**, 87–894.

20 E. Ionescu, C. Linck, C. Fasel, M. Muller, H. J. Kleebe and R. Riedel, Polymer-derived SiOC/ZrO_2 ceramic nanocomposites with excellent high-temperature stability, *J. Am. Ceram. Soc.*, 2010, **93**(1), 241–250.

21 E. Ionescu, C. Balan, H.-J. Kleebe, M. M. Müller, O. Guillon, D. Schliephake, M. Heilmaier, R. Riedel and V. Sglavo, High-temperature creep behavior of SiOC glass-ceramics: Influence of network carbon versus segregated carbon, *J. Am. Ceram. Soc.*, 2014, **97**(12), 3935–3942.

22 C. Linck, E. Ionescu, B. Papendorf, D. Galuskova, D. Galusek, P. Sajgalik and R. Riedel, Corrosion behavior of silicon oxycarbide-based ceramic nanocomposites under hydrothermal conditions, *Int. J. Mater. Res.*, 2013, **103**(1), 31–39.

23 T. Rouxel, G. D. Soraru and J. Vicens, Creep viscosity and stress relaxation of gel-derived silicon oxycarbide glasses, *J. Am. Ceram. Soc.*, 2001, **84**(5), 1052–1058.

24 P. Colombo, J. R. Hellmann and D. L. Shelleman, Mechanical properties of silicon oxycarbide ceramic foams, *J. Am. Ceram. Soc.*, 2001, **84**(10), 2245.

25 Y. Gou, X. Tong, Q. Zhang, B. Wang, Q. Shi, H. Wang, Z. Xie and Y. Wang, The preparation and characterization of polymer-derived Fe/Si/C magnetoceramics, *Ceram. Int.*, 2016, **42**(1), 681–689.

26 A. Saha and R. Raj, Crystallization maps for SiCO amorphous ceramics, *J. Am. Ceram. Soc.*, 2007, **90**(2), 578–583.

27 A. W. Weimer, K. J. Nilsen, G. A. Cochran and R. P. Roach, Kinetics of carbothermal reduction synthesis of beta siliconcarbide, *AIChE J.*, 1993, **39**(3), 493–503.

28 M. Adam, M. Wilhelm and G. Grathwohl, Polysiloxane derived hybrid ceramics with nanodispersed Pt, *Microporous Mesoporous Mater.*, 2012, **151**, 195–200.

29 B. García, E. Casado and A. Tamayo, Synthesis and characterization of Ce/SiOC nanocomposites through the polymer derived ceramic method and evaluation of their catalytic activity, *Ceram. Int.*, 2020, **46**(2), 1362–1373.

30 M. Hojamberdiev, R. M. Prasad, C. Fasel, R. Riedel and E. Ionescu, Single-source-precursor synthesis of soft magnetic Fe_3Si- and Fe_5Si_3-containing SiOC ceramic nanocomposites, *J. Eur. Ceram. Soc.*, 2013, **33**(13–14), 2465–2472.

31 Z. Yu, L. Yang, H. Min, P. Zhang, C. Zhou and R. Riedel, Single-source-precursor synthesis of high temperature stable SiC/C/Fe nanocomposites from a processable hyperbranched polyferrocenylcarbosilane with high ceramic yield, *J. Mater. Chem. C*, 2014, **2**(6), 1057–1067.

32 Z. Yu, P. Zhang, Y. Feng, S. Li, Y. Pei and R. Riedel, Template-free synthesis of porous Fe_3O_4/SiOC(H) nanocomposites with enhanced catalytic activity, *J. Am. Ceram. Soc.*, 2016, **99**(8), 2615–2624.

33 R. Harshe, C. Balan and R. Riedel, Amorphous Si(Al)OC ceramic from polysiloxanes: bulk ceramic processing, crystallization behavior and applications, *J. Eur. Ceram. Soc.*, 2004, **24**(12), 3471–3482.

34 M. Narisawa and Y. Abe, Microstructure of SiC–Si–Al_2O_3 composites derived from silicone resin – metal aluminum filler compounds by low temperature reduction process, *IOP Conf. Ser.: Mater. Sci. Eng.*, 2011, **18**(4), 042003.

35 L. Toma, C. Fasel, S. Lauterbach, H.-J. Kleebe and R. Riedel, Influence of nano-aluminum filler on the microstructure of SiOC ceramics, *J. Eur. Ceram. Soc.*, 2011, **31**(9), 1779–1789.

36 R. Q. Yao, Z. D. Feng, B. J. Zhang, Y. X. Yu and L. F. Chen, Synthesis and photoluminescence properties of continuous freestanding SiC(Al) films derived from aluminum-containing polycarbosilane, *Thin Solid Films*, 2010, **518**(24), e165–e168.

37 P. Zhang, J. Liang, K. Y. Wang and S. M. Guo, The formation of fibrous SiC in SiC/Al_2O_3 composites from the silica–carbon–aluminum system, *Int. J. Refract. Met. Hard Mater.*, 2012, **35**, 196–201.

38 E. Ionescu, C. Terzioglu, C. Linck, J. Kaspar, A. Navrotsky, R. Riedel and L. Gauckler, Thermodynamic control of phase composition and crystallization of metal-modified silicon oxycarbides, *J. Am. Ceram. Soc.*, 2013, **96**(6), 1899–1903.

39 C. Zhou, L. Yang, H. Geng, Q. Zheng, H. Min, Z. Yu and H. Xia, Preparation of Si–C–N–Fe magnetic ceramic derived from iron-modified polysilazane, *Ceram. Int.*, 2012, **38**(8), 6815–6822.

40 W. A. Eranezhuth, S. Sridar, B. K. Adhimoolam and R. Kumar, Ablation resistance of precursor derived Si–Hf–C–N(O) ceramics, *J. Eur. Ceram. Soc.*, 2016, **36**(15), 3717–3723.

41 E. Ionescu, B. Papendorf, H.-J. Kleebe, H. Breitzke, K. Nonnenmacher, G. Buntkowsky and R. Riedel, Phase separation of a hafnium alkoxide-modified polysilazane upon polymer-to-ceramic transformation—A case study, *J. Eur. Ceram. Soc.*, 2012, **32**(9), 1873–1881.

42 Y. Lyu, H. Tang and G. Zhao, Effect of Hf and B incorporation on the SiOC precursor architecture and high-temperature oxidation behavior of SiHfBOC ceramics, *J. Eur. Ceram. Soc.*, 2020, **40**(2), 324–332.

43 Q. Wen, Z. Yu, R. Riedel and E. Ionescu, Single-source-precursor synthesis and high-temperature evolution of a boron-containing SiC/HfC ceramic nano/micro composite, *J. Eur. Ceram. Soc.*, 2020, **44**(5), 3002–3012.

44 C. Zhou, X. Gao, Y. Xu, G. Buntkowsky, Y. Ikuhara, R. Riedel and E. Ionescu, Synthesis and high-temperature evolution of single-phase amorphous Si–Hf–N ceramics, *J. Eur. Ceram. Soc.*, 2015, **35**(7), 2007–2015.

45 N. Yang, M. Gao, J. Li and K. Lu, Nickel-containing magnetoceramics from water vapor-assisted pyrolysis of polysiloxane and nickel 2,4-pentanedionate, *J. Am. Ceram. Soc.*, 2019, **103**(1), 145–157.

46 P. Greil, Active-filler-controlled pyrolysis of preceramic polymers, *J. Am. Ceram. Soc.*, 1995, **78**(4), 835–848.

47 N. Yang and K. Lu, Thermophysical property and electrical conductivity of titanium isopropoxide – polysiloxane derived ceramics, *J. Eur. Ceram. Soc.*, 2019, **39**(14), 4029–4037.

48 Z. Yu, H. Min, J. Zhan and L. Yang, Preparation and dielectric properties of polymer-derived SiCTi ceramics, *Ceram. Int.*, 2013, **39**(4), 3999–4007.

49 H. D. Akkas, M. L. Ovecoglu and M. Tanoglu, Silicon oxycarbide-based composites produced from pyrolysis of polysiloxanes with active Ti filler, *J. Eur. Ceram. Soc.*, 2006, **26**(15), 3441–3449.

50 M. Hojamberdiev, R. M. Prasad, K. Morita, Y. Zhu, M. A. Schiavon, A. Gurlo and R. Riedel, Template-free synthesis of polymer-derived mesoporous SiOC/TiO_2 and SiOC/N-doped TiO_2 ceramic composites for application in the removal of organic dyes from contaminated water, *Appl. Catal., B*, 2012, **115–116**, 303–313.

51 R. Anand, S. P. Sahoo, B. B. Nayak and S. K. Behera, Phase evolution in Zr-doped preceramic polymer derived SiZrOC hybrids, *Ceram. Int.*, 2020, **46**(7), 9962–9967.

52 H. Laadoua, N. Pradeilles, R. Lucas, S. Foucaud and W. J. Clegg, Preparation of ZrC/SiC composites by using polymer-derived ceramics and spark plasma sintering, *J. Eur. Ceram. Soc.*, 2020, **40**(5), 1811–1819.

53 X. Long, C. Shao, H. Wang and J. Wang, Single-source-precursor synthesis of SiBNC-Zr ceramic nanocomposites fibers, *Ceram. Int.*, 2016, **42**(16), 19206–19211.

54 N. Wu, L. Y. Wan, Y. Wang and F. Ko, Conversion of hydrophilic SiOC nanofibrous membrane to robust hydrophobic materials by introducing palladium, *Appl. Surf. Sci.*, 2017, **425**, 750–757.

55 B. Zhao, H. J. Zhang, H. H. Tao, Z. J. Tan, Z. Jiao and M. H. Wu, Low temperature synthesis of mesoporous silicon carbide *via* magnesiothermic reduction, *Mater. Lett.*, 2011, **65**(11), 1552–1555.

56 Y. Pan and J. L. Baptista, Chemical instability of silicon carbide in the presence of transition metals, *J. Am. Ceram. Soc.*, 1996, **79**(8), 2017–2026.

57 W. Duan, X. Yin, C. Luo, J. Kong, F. Ye and H. Pan, Microwave-absorption properties of SiOC ceramics derived from novel hyperbranched ferrocene-containing polysiloxane, *J. Eur. Ceram. Soc.*, 2017, **37**(5), 2021–2030.

58 B. Du, J. Qian, P. Hu, C. He, M. Cai, X. Wang and A. Shui, Enhanced electromagnetic wave absorption of Fe-doped silicon oxycarbide nanocomposites, *J. Am. Ceram. Soc.*, 2019, **103**, 1732–1743.

59 K. Bawane, D. Erb and K. Lu, Carbon content and pyrolysis atmosphere effects on phase development in SiOC systems, *J. Eur. Ceram. Soc.*, 2019, **39**(9), 2846–2854.

60 H. J. Kleebe, C. Turquat and G. D. Soraru, Phase separation in an SiCO glass studied by transmission electron microscopy and electron energy-loss spectroscopy, *J. Am. Ceram. Soc.*, 2001, **84**(5), 1075–1080.

61 A. Schneider, Iron layer formation during cementite decomposition in carburising atmospheres, *Corros. Sci.*, 2002, **44**(10), 2353–2365.

62 C. Stabler, A. Reitz, P. Stein, B. Albert, R. Riedel and E. Ionescu, Thermal properties of SiOC glasses and glass ceramics at elevated temperatures, *Materials*, 2018, **11**(2), 279.

63 S. J. Widgeon, S. Sen, G. Mera, E. Ionescu, R. Riedel and A. Navrotsky, ^{29}Si and ^{13}C solid-state NMR spectroscopic study of nanometer-scale structure and mass fractal characteristics of amorphous polymer derived silicon oxycarbide ceramics, *Chem. Mater.*, 2010, **22**(23), 6221–6228.

64 A. H. Tavakoli, M. M. Armentrout, M. Narisawa, S. Sen, A. Navrotsky and R. Riedel, White Si–O–C ceramic: structure and thermodynamic stability, *J. Am. Ceram. Soc.*, 2015, **98**(1), 242–246.

65 E. Ionescu, S. Sen, G. Mera and A. Navrotsky, Structure, energetics and bioactivity of silicon oxycarbide-based amorphous ceramics with highly connected networks, *J. Eur. Ceram. Soc.*, 2018, **38**(4), 1311–1319.

66 K. Lu, D. Erb, K. Bawane and N. Yang, Comparison of traditional and flash pyrolysis of different carbon content silicon oxycarbides, *J. Eur. Ceram. Soc.*, 2019, **39**(10), 3035–3041.

67 J. A. Golczewski and F. Aldinger, Thermodynamic modeling of amorphous Si–C–N ceramics derived from polymer precursors, *J. Non-Cryst. Solids*, 2004, **347**(1–3), 204–210.

68 M. W. Chase Jr., *NIST-JANAF Thermochemical Tables*, American Institute of Physics, 4th edn, 1998.

69 C. Vakifahmetoglu, E. Pippel, J. Woltersdorf and P. Colombo, Growth of one-dimensional nanostructures in porous polymer-derived ceramics by catalyst-assisted pyrolysis. Part I: Iron catalyst, *J. Am. Ceram. Soc.*, 2010, **93**(4), 959–968.

70 F. J. Narcisco-Romero and F. Rodriguez-Reinoso, Synthesis of SiC from rice husks catalysed by iron, cobalt or nickel, *J. Mater. Sci.*, 1996, **31**, 779–784.

71 G.-W. Meng, L.-D. Zhang, Y. Qin, F. Phillipp, S.-R. Qiao, H.-M. Guo and S.-Y. Zhang, Chemical vapor deposition of beta-SiC nanowires on granular active carbon cylinders loaded with iron nanoparticles inside the pores, *Chin. Phys. Lett.*, 1998, **15**(9), 689–691.

72 J.-S. Lee, Y.-K. Byeun, S.-H. Lee and S.-C. Choi, *In situ* growth of SiC nanowires by carbothermal reduction using a mixture of low-purity SiO_2 and carbon, *J. Alloys Compd.*, 2008, **456**(1–2), 257–263.

73 G.-y. Li, X.-d. Li, H. Wang, X. Xing and Y. Yang, SiC nanowires grown on activated carbon in a polymer pyrolysis route, *Mater. Sci. Eng., B*, 2010, **166**(1), 108–112.

74 G.-Y. Li, X.-D. Li, H. Wang and L. Liu, Long SiC nanowires synthesized from off-gases of the polycarbosilane-derived SiC preparation, *Appl. Phys. A*, 2009, **98**(2), 293–298.

75 Y. Gao, Y. Bando, T. Sato and Y. Kitami, Needle-like SiC nanorods, *Jpn. J. Appl. Phys.*, 2001, **40**, 1065–1067.

76 Z. Liu, V. Srot, P. V. Aken, J. C. Yang and M. Rühle, Nanostructure characterization of iron catalyst assisted SiC nanowires, *Microsc. Microanal.*, 2007, **13**(S02), 754–755.

77 Y. Fu, Y. Zhang, X. Yin, T. Li and J. Zhang, Awl-like HfC nanowires grown on carbon cloth *via* Fe-catalyzed in a polymer pyrolysis route, *J. Am. Ceram. Soc.*, 2020, **103**(6), 3458–3465.

78 F. Wang, G.-Q. Jin and X.-Y. Guo, Formation mechanism of Si_3N_4 nanowires via carbothermal reduction of carbonaceous silica xerogels, *J. Phys. Chem. B*, 2006, **110**, 14546–14549.

79 P. Nikolopoulos, S. Agathopoulos, G. N. Angelopoulos, A. Naoumidis and H. Grobmeier, Wettability and interfacial energies in SiC–liquid metal systems, *J. Mater. Sci.*, 1992, **27**, 139–145.

80 B. Wang, M. Liu, Y. Wang and X. Chen, Structures and energetics of silver and gold nanoparticles, *J. Phys. Chem. C*, 2011, **115**(23), 11374–11381.

81 J. Lacaze and B. Sundman, An assessment of the Fe–C–Si system, *Metall. Trans. A*, 1991, **22**, 2211–2223.

82 S. N. Mohammad, Analysis of the vapor–liquid–solid mechanism for nanowire growth and a model for this mechanism, *Nano Lett.*, 2008, **8**(5), 1532–1538.